bioRxiv preprint doi: https://doi.org/10.1101/2022.07.11.499581; this version posted July 26, 2022. The copyright holder for this preprint (which was not certified by peer review) is the author/funder, who has granted bioRxiv a license to display the preprint in perpetuity. It is made available under aCC-BY-NC-ND 4.0 International license.

A Glass Phase Plate for Wavelength Sensitive Superresolution Microscopy

SANDUNI I. FERNANDO[1], JASON T. MARTINEAU[1], THIEN N. VU[3], BRIAN BAKER[4], ROB J. HOBSON[3], BRIAN MUELLER[3], RAJESH MENON[2], ERIK M. JORGENSEN[3], AND JORDAN M. GERTON[1,*]

[1] University of Utah Department of Physics and Astronomy, 201 James Fletcher Bldg. 115 S. 1400 E Salt Lake City, UT 84112-0830
[2] University of Utah Department of Electrical and Computer Engineering 50 S. Central Campus Drive, MEB Room 2110 Salt Lake City, UT 84112
[3] University of Utah School of Biological Sciences, 257 South 1400 East Salt Lake City, Utah 84112
[4] University of Utah Nanofab 36 S. Wasatch Drive, SMBB Room 2500 Salt Lake City, UT 84112
[*] Corresponding author: jgerton@physics.utah.edu

Compiled July 11, 2022

Precision in superresolution microscopy is dependent on the photon yield. Multicolor localization microscopy typically relies on bandpass filters and sequential imaging to distinguish fluorescent tags. By engineering the pointspread function with a spatial light modulator (SLM), the wavelength of specific fluors can be distinguished by their unique pattern on the camera face and can thereby increase photon budgets and be imaged simultaneously. Here, instead of an SLM, we insert a silicon-dioxide phase plate, the X-phase plate (XPP) in the Fourier plane of the detection path of a wide-field fluorescence microscope to engineer the PSFs (XPSF). We demonstrate that the XPSF can be used for hyper-spectral superresolution microscopy of biological samples. The XPSF achieves ∼25 nm in-plane resolution, ∼250 nm axial resolution and can distinguish three fluorescent probes with ∼80 nm peak separation between consecutive spectra at the vicinity of axial focus.

1. INTRODUCTION

Localization microscopy (LM) [1–11] - sometimes called Single Molecule Localization Microscopy (SMLM) - has transformed biological fluorescence microscopy over the past decade and a half. Techniques like PALM [12–15] and STORM [16–18], together with STED [19] and structured illumination [20], have overcome the optical diffraction limit imposed by classical microscopes. These new technologies have produced sharper images and videos of intracellular processes and interactions between proteins and organelles.

Within localization microscopy specifically, recent work has demonstrated that engineering the point-spread function in the detection path of a microscope can increase its utility – allowing for localization precision in the axial direction [21–27], dipole orientation measurement [28], temporal superresolution [29], and even spectral identification of the emission of the fluors. One method to engineer PSFs is to use a phase mask created by a liquid crystal spatial light modulator (LCSLM) in the Fourier plane of the detection path. Others have used gratings or phase ramps to introduce chromatic aberrations [30–34]. Furthermore, deep learning algorithms have been used to distinguish the emitters' spatial and spectral identity when using engineered PSFs [35]. In the long view, eliminating the need for spectral filters will improve localization microscopy by reducing the photon loss that accompanies such systems and importantly allow superresolution microscopy of living cells.

In this paper, we demonstrate that a glass phase plate can generate engineered PSFs with improved spectral identification and localization precision. Localization using the XPSF avoids the expense of the LCSLM and the ad-hoc computational complexity of deep learning approaches. The X-phase plate (XPP) is relatively simple to fabricate – and potentially inexpensive to manufacture at scale using standard masking and plasma-mediated vapor-etching technology. The XPP can operate across a wide span of numerical apertures and magnifications. By in-

bioRxiv preprint doi: https://doi.org/10.1101/2022.07.11.499581; this version posted July 26, 2022. The copyright holder for this preprint (which was not certified by peer review) is the author/funder, who has granted bioRxiv a license to display the preprint in perpetuity. It is made available under aCC-BY-NC-ND 4.0 International license.

serting it into the Fourier plane of a commercial microscope, we demonstrate that the engineered PSFs can be distinguished spectrally under simultaneous illumination without using spectral filters, to image microtubules and mitochondria in a fixed cell.

2. METHODS

A. Optical Setup

We conducted experiments on two different microscopes. The first microscope was a home-built inverted wide-field fluorescence microscope with four laser lines at 405, 488, 561, and 647 nm.

These lasers were co-aligned using successive long-pass dichroic filters passing through an acousto optic tunable filter (AOTF) to control the intensity of each. After the AOTF, all laser lines were coupled into a single multimode patch cable to transfer the laser power from our laser bench to the bench on which the microscope was constructed. A detailed diagram of this setup is given in the supplementary material (see Supplement 1). However, it is functionally similar to the diagram in Fig. 1, representing the layout of the second microscope – Vutara 352 commercial microscope.

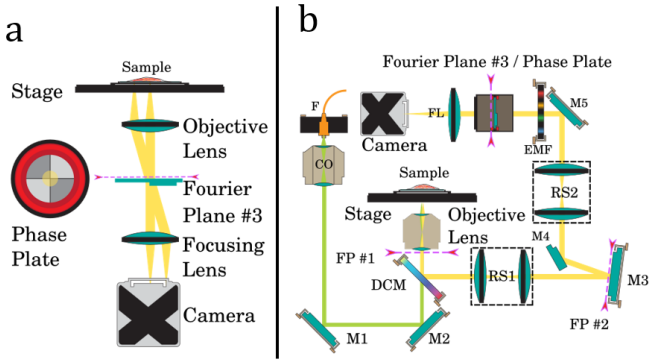

Fig. 1. Optical setup of the microscope. a) A very simplified diagram of the detection path of our microscope. b) A more detailed diagram of a Vutara 352 superresolution microscope. Fourier planes are indicated by magenta dashed lines. Labels are as follows: **F**: fiber out-couple; **CO**: collimation objective; **M1**, **M2**, **M3**, **M4**, **M5**: silver mirrors **DCM**: dichroic mirror; **FP #1**, **FP #2** Fourier planes; **RS1**, **RS2**: relay lens systems; **EMF** emission filter; **FL** focusing lens.

In both microscopes, we modified the PSF to be sensitive to different spectra using a specially designed glass phase plate placed in one of the Fourier planes of the collection path. The phase plate was manufactured with plasma-enhanced chemical vapor deposition process in the Nanofab facility of University of Utah. Manual adjustments to the phase plate placement at the Fourier plane were sufficient to ensure that the resulting PSF was symmetric and translationally invariant enough to be useful – the sensitivity of this placement was about a millimeter.

B. Working Principle

The phase plate's geometry consists of four quadrants, with each diagonal pair having the same thickness. One advantage of our design is that the phase pattern created on the detected signal by the phase plate is essentially unchanged by differences in numerical aperture and magnification because its features only change in the angular polar coordinate direction. This quality makes it practically useful to a broad range of microscope designs.

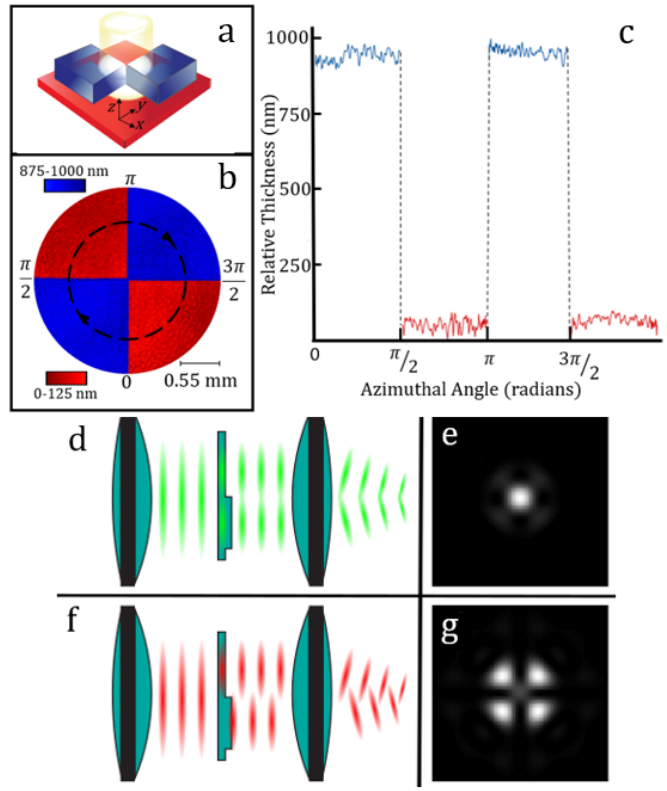

Fig. 2. Twyman-Green laser interferometer data and the working principle behind the phase plate. a) A schematic of the phase plate. The blue regions are SiO_2 depositions on top of a thin glass plate colored red. The emission light beam is incident on the phase plate at its center as indicated by the bright spot. b) A color-coded height map of an approximately 2 mm diameter section of the phase plate's center in the xy plane measured by the Twyman-Green interferometer, as a thickness difference from a nominal zero. c) The height profile along the dashed black circle in z axis. The origin of (b) coincides with the origin of (c) and the azimuthal angle is measured clockwise as indicated by the arrows in (b) along the dashed line. The working principle of our phase plate is shown in panels d) to g). Panels d) and f) show how the phase plate affects fluorescence light of different wavelengths (green and red respectively). e) and g) show the respective PSFs (simulated).

We measured the surface profile of the phase plate as shown in Fig. 2, using phase-shifting interferometry on a Twyman-Green interferometer. The blue quadrants are about $\Delta_t = 960 \pm 20$ nm thicker than the lighter red quadrants. The effect of the $\Delta_t = 960$ nm step is illustrated in Fig. 2(d)-(g). Figure 2(d) shows green light ($\lambda = 500$ nm) propagating through the phase plate, placed in the Fourier plane of an imaging system. In these panels , the top half of the phase plate is drawn as a thin quadrant. As the fluorescence passes through a thin quadrant (top), it is delayed in phase less than light passing through the thick quadrant (bottom). However, for this wavelength of light, the delay corresponds to a phase difference of about 2π, leaving the wave-front effectively flat. This means that when the light is focused on a detector by the imaging lens, the PSF is essentially identical to an Airy disk, as shown in Fig. 2(e).

bioRxiv preprint doi: https://doi.org/10.1101/2022.07.11.499581; this version posted July 26, 2022. The copyright holder for this preprint (which was not certified by peer review) is the author/funder, who has granted bioRxiv a license to display the preprint in perpetuity. It is made available under aCC-BY-NC-ND 4.0 International license.

By contrast, for $\lambda = 680$ nm light, a phase shift of half a wavelength between the two regions of the phase plate occurs (Fig. 2(f)). When this signal is focused onto a detector, destructive interference resulting from the phase discontinuity at the center of the PSF produces the cross-shaped null shown in panel (g). Hereafter, we refer to the PSF shapes in panels (e) and (g) as the *canonical forms* of our PSF. For wavelengths in between the above wavelengths, the PSF is a superposition of the two canonical forms in different proportions depending on the wavelength. As wavelength increases from the green canonical form to the red one, the intensity migrates outward along crossing diagonal lines from the center of the PSF. Because of this particular geometry, we refer to this PSF as the "XPSF". Similarly, we refer to the phase plate as the "X-phase plate" (XPP).

The detection path of both our open laser bench and commercial microscopes was modified by placing the XPP placed in a home-built phase plate at the last Fourier plane before the camera, as shown in Fig. 1(b). The mount fabrication process is described in the supplementary material (see Supplement 1); briefly, it is a 3D printed mount to hold the phase plate inside a 1" diameter 1" long lens tube. Successful phase plate placement in the Fourier plane did not require any fine-adjustment mechanisms. The module's installation took about 15 minutes total before each imaging experiment.

It is important to position the phase plate at the Fourier plane [4, 25, 36]. Figure 1(a) shows a greatly simplified diagram of the detection arm of our microscope. Two parallel bundles of rays are shown passing through the phase plate from two different emitters on the sample. They pass through the Fourier plane at the same place on the phase plate, rendering the PSFs detected on the camera translationally invariant. With our current optical path, placing the phase plate at another position along the detection path other than a Fourier plane would not achieve this desirable characteristic. However, it might be possible to increase the planar localization precision of a microscope PSF by intentionally introducing translational variance in the signal by placing a phase plate near to – but not at – the Fourier plane.

C. Numerical Analysis

We wrote a custom library of classes and scripts in MATLAB to analyze our raw multi-color localization microscopy data as described below.

C.1. PSF model

Others have modeled the PSF by vector-based diffraction [30, 31]. However, the scalar diffraction theory was sufficient to describe the XPSF. We modified the Gibson-Lanni PSF model with a term representing the phase pattern imparted by the XPP to fit the signal PSFs in our data. This modification is shown in Eq. 1 below:

$$U = \exp\left(\frac{i2\pi\left(n_a - n_p\right)\Delta_t\Theta(D)}{\lambda} + \psi_{GL}(D)\right)$$
$$XPSF(x,y) = \mathcal{A}\int_D U^* U \tag{1}$$

where: ψ_{GL} represents the standard phase terms in the Gibson-Lanni PSF model [37]; Δ_t is the step height of the phase plate – the difference in thickness between the thick and thin regions of the phase plate; n_a and n_p are the indices of refraction for air and the phase plate, respectively; Θ describes the topography of the phase plate and its maximum value is normalized to unity; The integral is taken over the unit disk, D, which represents the illuminated portion of the Fourier plane;$\mathcal{A}$ is a normalization constant such that the integral of the XPSF is unity; Finally (x, y) is a point in the image plane of the microscope.

C.2. Evaluating the diffraction integral

Fast-Fourier transforms (FFTs) can efficiently calculate a simplification of the diffraction integral representing light propagation of a PSF-engineered microscope [24]. However, we found that padding the numerical representation of the Fourier plane with zeros to increase the FFT sample rate to match the camera's pixel size was too slow for our analysis goals. Instead, we calculated the diffraction integral using a Gaussian cubature formula of the unit disk as given by Cools *et al.* [38] with the topography of the phase plate being modeled using sigmoid functions.

C.3. Calibration for Zernike aberrations

Accounting for the optical aberrations inherent in our microscope was essential for matching the measured PSF and our model PSF. We used a maximum likelihood estimation algorithm to fit the first fourteen Zernike polynomials as a component of ψ_{GL} to a measurement of the XPSF measured through two or three wavelength windows (depending on the number of fluorescent emitter types in the sample), defined by the filter set of the microscope and the test point-emitters used in the calibration. The point emitters were Tetraspeck beads from ThermoFisher illuminated with 488, 561, and 647 nm laser lines (Yellow-Green, Orange, and Dark-Red emission spectra). The data set was fitted to model PSFs corresponding to their respective wavelength and spatial coordinates to extract the vector of Zernike weights characteristic of the aberrations from the microscope. We used a monochromatic representation of the corresponding spectra at their peak wavelength with a Gaussian blur.

C.4. Maximum Likelihood Estimation

With a model of the XPSF in hand, emitter localization and wavelength estimation are done in two steps. The first step is to find a guess for the emitter wavelength, lateral position on the camera, and depth position in the sample. The XPSF is sensitive enough to the axial position of the emitter that this parameter must be taken into account immediately. We make this guess by constructing a lookup table, using the above PSF model that was calibrated to the specific Zernike aberrations inherent in the system. The lookup-table has four dimensions: x, y, and z spatial dimensions and a spectral dimension λ. The spatial dimensions of the lookup-table consist of the PSF model at positions separated by 50 nm in-plane and 50 nm axially, while the spectral dimension consists of two (or three) monochromatic representations of the calibrated PSF.

The guessed values become the initial point for the second localization by minimizing the negative loglikelihood of the signal with respect to the model using a Nelder-Mead simplex algorithm [39]. This fit is done with all four dimensions of the PSF (x, y, z, and λ) but with λ limited by $\pm$ 20 nm from the guess. During this part of the analysis, a monochromatic model of the PSF is used because fitting using Nelder-Mead algorithm with a polychromatic representation of the PSF is too computationally costly. Nevertheless, a Zernike calibrated monochromatic PSF at the spectral center of mass of the corresponding spectrum with a Gaussian blur was a close enough representation to the data PSFs for the wavelength range we performed our imaging and the level of overlap between the spectra. We found the Nelder-Mead algorithm to be computationally faster than the Newton-Raphson method because the latter required calculating the Hessian of the objective function.

bioRxiv preprint doi: https://doi.org/10.1101/2022.07.11.499581; this version posted July 26, 2022. The copyright holder for this preprint (which was not certified by peer review) is the author/funder, who has granted bioRxiv a license to display the preprint in perpetuity. It is made available under aCC-BY-NC-ND 4.0 International license.

After each fit has gone through 100 iterations, the simplex algorithm is terminated, and the fit is evaluated against the data using a likelihood ratio test. The result is passed to the rendering software (Vutara SRX) to produce images with varying statistical filtering criteria. The user can dynamically choose a p-value during the rendering process to qualitatively optimize the reconstructed superresolution image.

D. Sample Preparation and Imaging

D.1. Fluorescent Bead Sample Preparation

The samples imaged in Figures 3 and 4 were made by diluting ThermoFisher FluoSphere beads (see results for more specific information) in a 1:10^4 ratio from a stock solution in ultra-pure water. A microscope slide was prepared with 15 μl of poly-L-lysine as an adhesive for the beads and was allowed to stand on the slide for ten minutes before any excess was pipetted off. 20 μl of the dilute bead solution was then pipetted onto the slide and dried in a vacuum chamber. Once dry, the area containing the beads was secured with a coverslip using nail polish as a sealer. The sample was mounted on the microscope such that the laser light is incident through the coverslip, which is thinner.

D.2. Biological Sample Preparation

U2OS cells grown in #1.5H ibidi chambers (μ-Slide 8 well Cat# 80826) were fixed in 37 ^{o}C 3% paraformaldehyde (EMS) and 0.1% glutaraldehyde (EMS) in PEM buffer 100 mM PIPES, 1 mM EGTA, 1 mM $MgCl_2$, pH 7.0) for 15 minutes. Glutaraldehyde autofluorescence was quenched by adding 0.1% sodium borohydride in PBS for 7 minutes. Cells were blocked and permeabilized in blocking buffer (10% donkey serum and 0.2% triton-X 100 in PBS) for 45 minutes at room temperature. Cells were incubated in primary antibodies in blocking buffer. Cells were incubated with rabbit anti-Tomm20 (abcam AB78547) and mouse anti-HSP60 (R&D systems MAB1800) (Thermo-Fisher) or with mouse anti-alpha tubulin (Sigma) and rabbit anti detyrosinated tubulin (Sigma). Cells were incubated overnight at 4 ^{o}C with shaking. Cells were washed 3 to 5 times in PBS. Cells were incubated in secondary antibodies anti-rabbit Alexa Fluor 647 (Thermo-Fisher), anti-mouse CF568 (Biotium) and Phalloidin-Alexa Fluor 488 (Thermo Fisher) for 1 hour at room temperature. Cells were washed 3 to 5 times in PBS. Cells were postfixed in 4% PFA for 5 minutes at room temperature and washed 3 to 5 times in PBS. Cells were imaged in standard Gloxy imaging buffer for dSTORM. photoswitching buffer comprised of 20 mM cysteamine, 1% (v/v) 2-mercaptoethanol and oxygen scavengers (glucose oxidase and catalase) in 50 mM Tris-10 mM buffer at pH 8.0.

3. RESULTS

A. Ability to Distinguish Between Spectra

To demonstrate the ability of the XPSFs to distinguish between spectra, we used a phase plate with a 660 nm step height (XPP1), similar to the one shown in Fig. 2 that generates PSFs in the XPSF family. We illuminated three different species of fluorescent beads (Thermo Fisher FluoSpheres: Dark-Red, Orange and Yellow-Green, prepared as described above) with 647, 561, and 488 nm laser lines. Each localization was determined using ~6000 photons. By comparing the wavelengths estimated using our MATLAB algorithm, indicated by the color-coded wavelength values and boxes in Fig. 3(a) (simultaneous illumination) to the control panels (b), and (d) (single line illumination), it is clear that the estimation program correctly identifies the different fluorescent bead species near the axial focus.

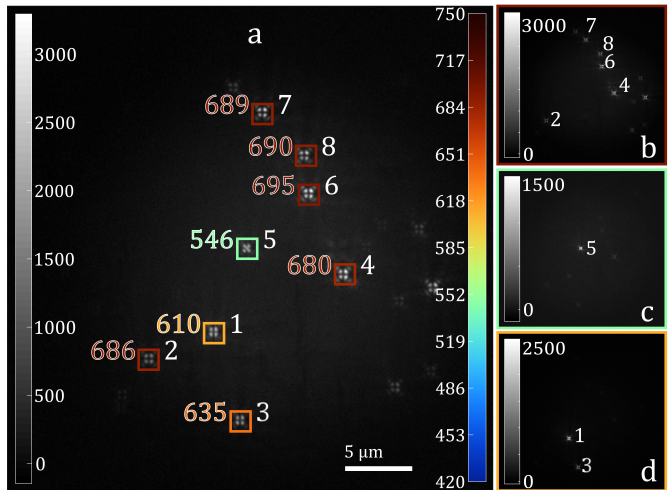

Fig. 3. Experiment to distinguish different spectral species of fluorescent beads using only the shape of the XPSF. a) Three different species of beads imaged simultaneously. Colored boxes are drawn around each PSF with a number indicating the wavelength to which each was localized. The gray-scale color bar indicates photon counts, and the right color bar indicates wavelength. Each PSF is numbered $1-8$. b) and d) The same sample illuminated only with 647, 561, 488 nm respectively.

B. Localization Precision

We then tested whether the phase plate could distinguish fluors illuminated by a single laser (Fig. 4). For this experiment, we used XPP2 with a step height of 960 nm and calculated the localization precision and the ability to distinguish between spectra near $z = 0$. XPP2 produced a greater change in structural features of the PSFs among the three bead spectra and spatial coordinates than XPP1. We captured $1,000$ camera frames under simultaneous laser illumination and fitted the data PSFs using our MATLAB program. The XPSF demonstrates an in-plane spatial localization precision of about 10 nm (FWHM) near $z = 0$. The spectral localization precision is about 10 nm at ~6000 photons, which is sufficient to overcome the cross-talk among the respective spectra.

C. Multi-Spectral Superresolution

The spectral detection of the XPSF can be used for biological imaging. Figure 5 shows a superresolution dSTORM image of microtubules (green), and TOMM20 (pink) in fixed U2OS cells. The localizations were plotted, using the XPSFs created by the XPP2 phase plate placed at the last Fourier plane of the Vutara 352 microscope. The cell sample was *illuminated simultaneously* by the 640 and 561 nm laser lines *without any emission filters*, and the spectra were localized only based on PSF shape. The excitation intensity for the two laser lines was ~5 kW/cm^2. A 405 nm laser was used at ~1 W/cm^2 to control the fluorophore blinking rate by driving the fluors in the dark excitation states back to the ground state. The two protein species are uniquely identifiable. TOMM20, which is incorporated into the outer membrane of the mitochondria, appears inter-woven within the microtubule forest as expected.

bioRxiv preprint doi: https://doi.org/10.1101/2022.07.11.499581; this version posted July 26, 2022. The copyright holder for this preprint (which was not certified by peer review) is the author/funder, who has granted bioRxiv a license to display the preprint in perpetuity. It is made available under aCC-BY-NC-ND 4.0 International license.

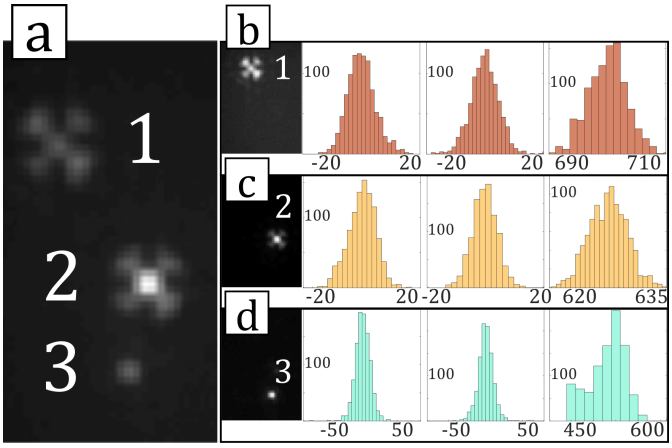

Fig. 4. Simultaneous spatial and spectral localization of three different fluorescent bead species. a) A sample of three beads illuminated by the three laser lines simultaneously. b) The same sample illuminated by only 647 nm light. The histograms show the distributions of localizations in x,y,λ, from left to right, with the horizontal axis in nm. c) and d) are similar to panel (a) corresponding only to 561 and 488 laser lines respectively.

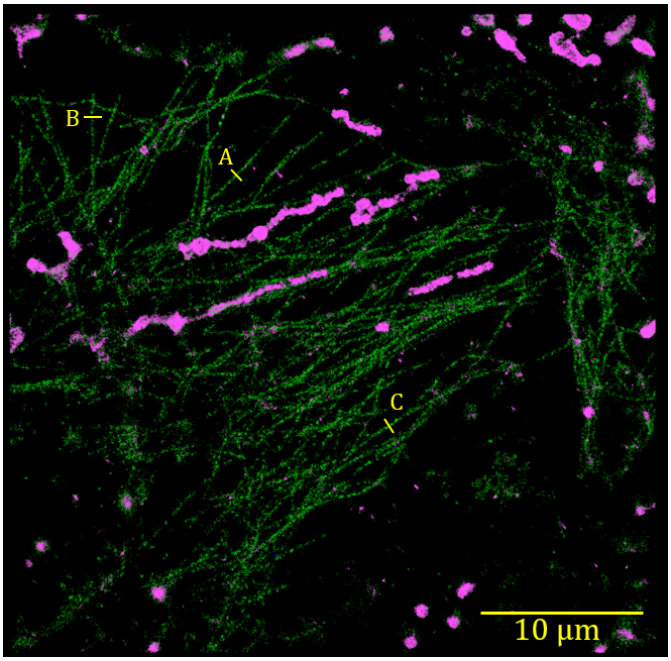

Fig. 5. Two color fixed cell imaging. Tubulin, labeled with Alexafluor 647, is rendered in green; TOMM20, labeled with CF 568, is rendered in pink. Line profile indicated by yellow, lines **A-C** are shown in detail in Fig. 6. The cell sample was illuminated simultaneously by the 640 and 561 nm laser lines without any emission filters, and the spectra were localized only based on PSF shape.

Microtubules provide an excellent reference to test the resolution in localization microscopy because of their extended linear nature and their known width. Figure 6 shows histograms indicating the density of localizations across three microtubule strands in Fig. 5 (A,B, and C) and a Gaussian function fit to each profile. To estimate our localization precision, we can compare

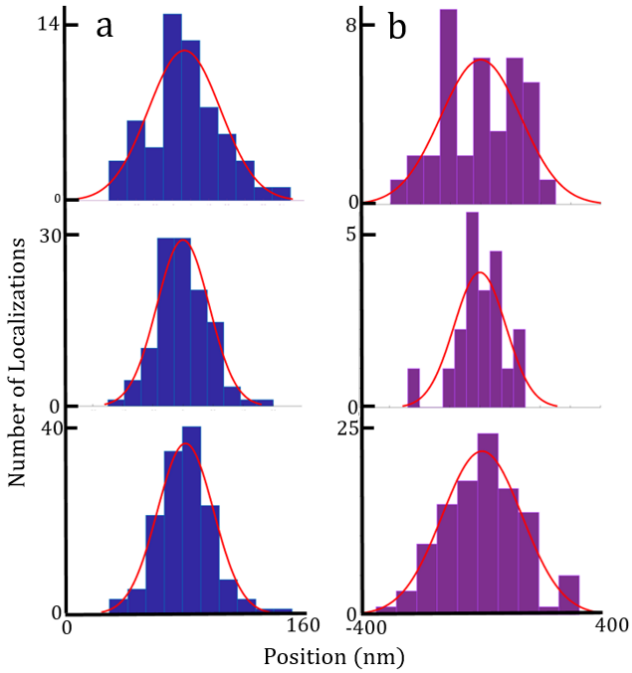

Fig. 6. The density of localizations along A,B, and C line segments of microtubules in Fig. 5. (a) Blue histograms indicate the density of localizations across the width (xy plane) and (b) purple histograms the depth (z) of a microtubule respectively along the line segments in Fig. 5 corresponding to line segments A, B, and C from top to bottom. The Gaussian fits to the histograms are in red. For the width (blue) histograms, the FWHM are 56, 51, and 41 nm from top to bottom and for the depth (purple) histograms, 314, 201, and 319 nm respectively.

the diameter of microtubules estimated from the FWHM in our image to the known diameter of 25 nm. The FWHM of these fits are between $41-56$ nm in the xy plane and $201-319$ nm in z direction. Even without considering the size of the anti-tubulin antibody, the results indicate a localization precision in fixed cells of about $15-30$ nm in-plane and about $180-300$ nm in the z plane.

4. DISCUSSION

A key goal in cell biology is to observe the movement of multiple proteins in a living cell at a spatial dimension meaningful to a protein – specifically at the diameter of a typical protein, ~10 nm. Here, we observe that XPSFs created by a four quadrant glass phase plate can be used for multi spectral imaging with localization precision comparable to other PSF families such as the Tetrapod and Double-Helix. The discussion below evaluates the localization precision of the XPSF, its ability to distinguish spectra, and its utility for imaging multiple probes under simultaneous excitation and detection.

A. Localization Precision and Bias

A key goal for PSF engineering is to localize the PSFs with higher precision than ~40 nm. First, we will use the Cramér-Rao lower bound (CRLB), referred to as σ^2_{min} in this paper, to measure the precision of the XPSF in the x, y, z, and λ dimensions. Then, we will discuss how we minimized the artifacts that can occur when estimating the z coordinates of the localizations.

bioRxiv preprint doi: https://doi.org/10.1101/2022.07.11.499581; this version posted July 26, 2022. The copyright holder for this preprint (which was not certified by peer review) is the author/funder, who has granted bioRxiv a license to display the preprint in perpetuity. It is made available under aCC-BY-NC-ND 4.0 International license.

We represent the center coordinates of a PSF at the image plane of the microscope as x_0 and y_0, the axial coordinate at the sample as z_p, and a representative wavelength for the emission spectra as λ. As others have noted, [6, 21, 40–43] it is calculated by inverting the Fisher information matrix and taking its diagonal elements as the minimum possible variance ($\sigma^2_{\min} = [\sigma^2_{\min,x_0}, \sigma^2_{\min,y_0}, \sigma^2_{\min,z_p}, \sigma^2_{\min,\lambda}]$) around the actual value that can be achieved when measuring the unknowns x, y, z, and λ. Assuming shot noise only, the Fisher information matrix I_k is given by Eq. 2 where μ_k is the theoretical (model) XPSF, and $\vec{\theta} = (x_0, y_0, z_p, \lambda)$ are the parameters being estimated:

$$I_k(\vec{\theta}) = \left[\frac{1}{\mu_k} \frac{\partial \mu_k}{\partial \theta_i} \frac{\partial \mu_k}{\partial \theta_j} \right]. \tag{2}$$

The theoretical precision in $\vec{\theta}$ for the XPSFs calculated as the $\sqrt{CRLB}$ (without considering optical aberrations) at three different emission wavelengths are shown in Fig. 7. Panels (a)-(c) show the calculations for $\lambda = 680$, 595, and 515 nm respectively. These wavelengths roughly correspond to the estimated wavelengths for FluoSpheres spectra for"Dark-Red", "Orange", and "Yellow-Green" in Fig. 4. For this calculation, we simplified the conditions by assuming that the number of photons per PSF can be determined exactly, the observed PSFs are not distorted from the model because of the Poissonian nature of light detection, and the background per camera pixel is uniform across all the pixels. We observed 1,000-5,000 photons per PSF during the fixed cell imaging experiment, with an average of about 2,500 photons. Figure 7 suggests that the axial localization precision is expected to be the best at the focal plane and that a higher z precision for Yellow-Green and Orange PSFs could be achieved than that of Dark-Red (about 30 vs. 50 nm). It should be noted that axial localization precision is significantly lower than that of the in-plane localizability of the XPSFs. The background level for the dSTORM image in Fig. 6 was as high as about 400 photons per pixel for which the CRLB for axial precision is around 120 nm.

We identified spectral and spatial values for the XPSFs in a two-step process: first, by accounting for Zernike aberrations in our optical set-up and second, by using a maximum likelihood estimation as described in Section C.4 of the Methods. Artifacts such as banding of localizations in the z direction (see Supplement 1) and mislocalizations in x, y, z, and λ can be minimized by fine tuning the optical elements in the microscope such that the Zernike aberrations in the XPSFs are a minimum. The localizations are then fit to the model XPSFs. To improve the localization precision further, we found that it is important to calibrate the model XPSFs in the lookup-table for optical aberrations: The models must closely resemble the optical data, the look-up tables for axial localizations must be sufficiently dense, and the fitting algorithm must be performaed iteratively to narrow in on the optimal localization during the analysis.

B. Simultaneous Multicolor Imaging

To provide cellular context, we must image multiple proteins tagged with different fluorophores. Usually, these fluorophores are excited one at a time in a sequence and tag-identified using emission filters. However, since XPSFs themselves contain information about the probe species, we can stimulate and image multiple probes simultaneously without using emission filters.

There are at least two additional challenges associated with simultaneous multicolor imaging: reducing background and

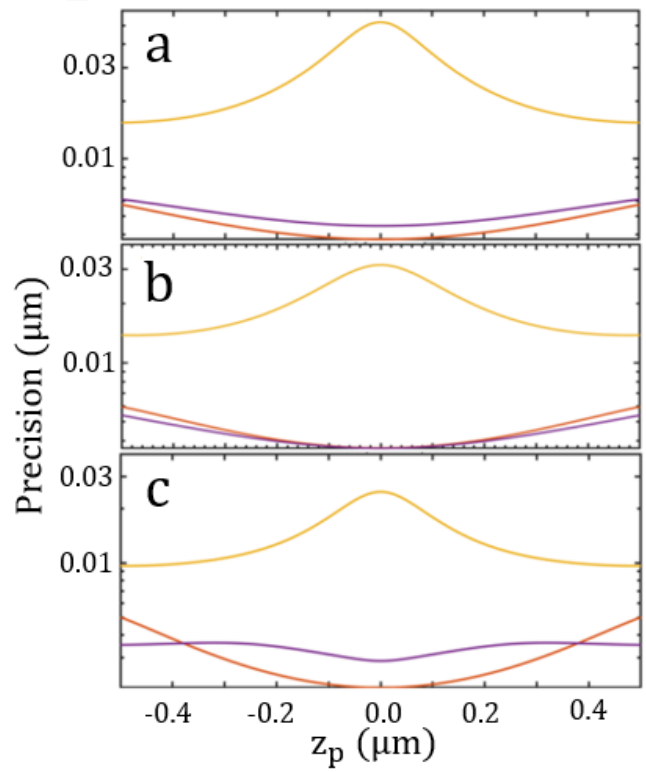

Fig. 7. Theoretical precision of the XPSF as a function of position relative to the focal plane, z_p, at different wavelengths for 3,000 photons per PSF. The wavelengths are 700 nm (a), 630 nm (b), and 500 nm (c). The yellow, red, and purple curves correspond to axial direction, the in-plane directions, and the wavelength respectively.

controlling blinking rates of fluors. First, since all fluorophore species are illuminated simultaneously and the emission is not separated spectrally, the structure of the XPSF can be obscured. The background fluorescence can arise from a different fluorescent species, from the same species but displaced emitters, or from autofluorescence from the cell. Any of these sources of fluorescence will make the structure of the XPSF harder to discern and will limit spectral separation of individual emitters. Thus, a fluorophore with significantly weaker brightness compared to others in the vicinity may get lost in the background and make it difficult or impossible for the fitting algorithm to converge on a solution.Theoretically, limiting blinking rates and editing out poor wavelength localizations could limit such miscalls.

The second challenge is controlling the independent blinking rates. To restore fluors to the ground state, we use a 405 nm laser for all fluorophores. But, the photophysics of the fluorophore and the density of the protein for each probe may require a different 405 nm laser intensity to optimize blinking. Highly concentrated clusters of a protein and unstable triplet states can lead to regions that are not sufficiently sparse to localize individual PSFs. Matching labeling densities might require diluting the fluorescent labels of particular proteins.

The benefits of simultaneous multicolor imaging is that it opens the possibility of imaging living cells. Currently, exhaustive imaging of protein localizations using filter sets can require minute-long acquisitions. Proteins and organelles can move during the acquisition. However, simultaneous imaging can identify

bioRxiv preprint doi: https://doi.org/10.1101/2022.07.11.499581; this version posted July 26, 2022. The copyright holder for this preprint (which was not certified by peer review) is the author/funder, who has granted bioRxiv a license to display the preprint in perpetuity. It is made available under aCC-BY-NC-ND 4.0 International license.

proteins as they interact or co-migrate in a cell. In addition, it might be possible to design a labeling scheme whereby different fluorophore species with tightly spaced emission spectra could be excited with a single laser line and still be separated spectrally. Imaging with a single laser will be less expensive and less damaging to the biological samples than illuminating with multiple laser lines (as was done here). The goal is to identify spectra at nanometer-scale spatial resolution at millisecond-scale temporal resolution, for long timespans of cellular behavior.

C. Performance of the XPSF

The disadvantage to engineered point spread functions relative to conventional localization microscopy is that localizations are very sensitive to the photon budget. First, there is inherently more fluorescence noise with simultaneous imaging, and second, the photons are distributed more broadly across camera pixels than with an Airy disk. The limits of XPSF imaging versus conventional localization microscopy can be modeled from experimental data.

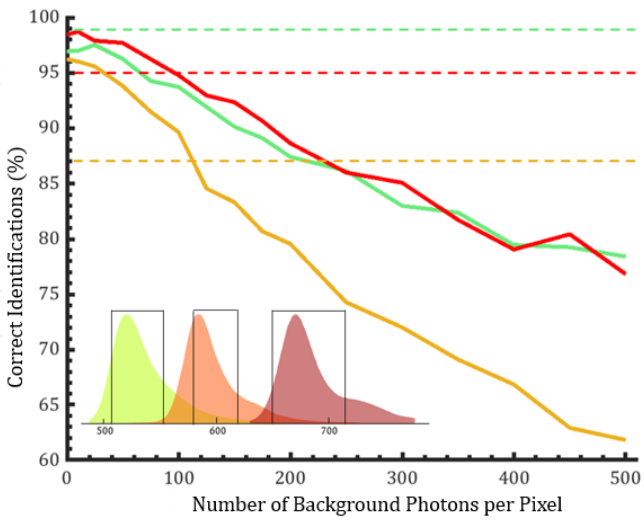

Fig. 8. Spectral discernibility of the XPSFs using a Monte-Carlo simulation. The percentage of correct spectral identifications for the probes AXF 647 (red), CF 568 (orange), and AXF 488 (green) are are plotted as a function of the number of background photons per camera pixel. In the simulations, We used a distribution of photons similar to the photon distribution observed in Fig. 5 with an average of 2,500 photons per PSF. The dotted lines indicate the theoretical spectral discernibility of emission filters color-coded the same as the dyes. The three spectra are at the bottom left with the transmission windows of the dichroic filter denoted by the black lines.

In Fig. 8 we simulated correct spectral assignments for the XPSF as a function of the number of background photons per pixel for the three dyes AXF 647, CF 568, and AXF 488, analogous to the emission spectra of the beads. The simulated sample background is extracted from multicolor images (e.g., Fig. 5) and is primarily caused by autofluorescence and fluorescence from out-of-focus emitters, both belonging to the same, or to different probe species. We simulated noisy XPSFs by incorporating the sample background, shot noise in photon detection, and camera noise to the model XPSFs at multiple spatial coordinates for a specific probe. Furthermore, we employed the same localization algorithm used for biological data analysis (Fig. 5) to determine the probe type. We used a distribution of photons similar to the photon distribution observed in Fig. 5 with an average of 2,500 photons per PSF. The number of correct identifications per spectrum is the number of XPSFs correctly sorted by the algorithm as a percentage of the total number of input XPSFs belonging to that probe. For a background of 100 photons per pixel, correct identifications for AXF647, CF568, and AXF488 probes were 92%, 85%, and 70%, respectively.

We also include a best-case scenario using spectral filters for comparison with XPSFs. In particular, we calculated the expected cross-talk between different spectral channels when using the combination of dichroic and long-pass filters in our commercial microscope (indicated by the transmission profiles in the inset to Fig. 8), and then subtracted this from unity to deduce the probability for a correct identification of fluorophore species. We did not take into account spectral or shot noise when making this best-case calculation, and we assumed that all three fluorophore species emit with the same peak intensity. The results of this calculation are indicated by the horizontal dashed lines in Fig. 8.

To obtain similar data from a cellular imaging experiment to compare to the simulation, we first sequentially illuminated fixed U2OS cells with the three laser lines and identified the fluorophore species using emission filters. Then, we applied our XPSF analysis algorithm to the same sequential data set, and extracted the fluorophore species from the shape of each PSF. For a background of ~ 100 photons per pixel, identifications were correctly reported for 92%, 85%, and 70% of the localizations for AXF647, CF568, and AXF488, respectively. This is a somewhat worse performance than predicted from the simulations (Fig. 8), particularly for AXF 488 which differed by 87% correct in the simulation vs 70% correct when measured. Truth tables for the simulations and the control experiment can be found in the supplemental section (see Supplement 1). The mismatch between the simulation and the actual data could be due to several factors. For example, it is difficult to precisely know the number of photons per PSF in the experimental data as has been reported elsewhere [44]. In addition, it is difficult to characterize the optical aberrations of the microscope, which leads to inaccurate model XPSFs. Other factors include variations in the background over the region of interest and having multiple (overlapping) PSFs in the same region of interest.

Nevertheless, using an algorithmic approach to localize engineered PSFs can be simpler and easier to implement when compared to deep learning methods. Unlike a LCSLM, our phase mask is a transmissive, polarization insensitive, and an inexpensive glass optic that can be easily inserted into a commercial microscope, as was done here. The XPSF models are evaluated at only 88 points (Gaussian Cubature model) which is computationally inexpensive. The PSF shapes are mathematically calculated for each x, y, z coordinate combination with the prior knowledge of the emission spectra, which eliminates the need of acquiring training data for every new set of conditions. However, calibrating the PSF model to closely resemble the data is challenging since many predetermined parameters (refractive indices, phase plate topography, spectra, and magnification) are involved.

5. CONCLUSION AND FUTURE WORK

A four-quadrant glass phase plate can adequately manipulate the structure of PSFs to differentiate three fluorescent emitters for localization microscopy. We use the scalar Gibson-Lanni model

bioRxiv preprint doi: https://doi.org/10.1101/2022.07.11.499581; this version posted July 26, 2022. The copyright holder for this preprint (which was not certified by peer review) is the author/funder, who has granted bioRxiv a license to display the preprint in perpetuity. It is made available under aCC-BY-NC-ND 4.0 International license.

with Gaussian cubature representation of the phase plate topography and the log-likelihood estimation to localize the emitters. Overall, our approach is adaptable to various microscopy methods. The XPSF, which results from placing the phase plate in the Fourier plane of the detection arm of a microscope, allows single molecules to be localized with a precision of 25 nm laterally and 250 nm axially. Additionally, proof-of-principle measurements using dye-doped beads suggests that with sufficient signal, it could be possible to resolve 10 nm spectral differences at the focal plane using our XPSF approach. We have demonstrated simultaneous imaging of two-color fixed U2OS cells with the XPSF.

One goal for future work is to improve the model PSFs to better account for aberrations and spectral factors, making our approach more robust and precise. Optimal PSFs would be capable of differentiating between similar spectra [45, 46] using a single laser to reduce phototoxicity. The eventual goal is to localize multiple proteins in three dimensions in a living cell. Only then will biologists be able to characterize protein movement and interactions at a scale that is meaningful to a cell.

See Supplement 1 for supporting content.

REFERENCES

1. H. Mazidi, A. Nehorai, and M. D. Lew, "A robust statistical estimation (rose) algorithm jointly recovers the 3d location and intensity of single molecules accurately and precisely," in *SPIE BiOS*, , vol. 10500 (SPIE), p. 11.
2. A. Dupont and D. C. Lamb, Nanoscale **3**, 4532 (2011).
3. S. Stallinga and B. Rieger, Opt. Express **18**, 24461 (2010).
4. S. Stallinga, "Single emitter localization analysis in the presence of background," in *SPIE Optical Systems Design*, , vol. 9630 (SPIE), p. 7.
5. M. Štefko, B. Ottino, K. M. Douglass, and S. Manley, Opt. Express **26**, 30882 (2018).
6. A. Tahmasbi, E. S. Ward, and R. J. Ober, Opt. Express **23**, 7630 (2015).
7. J. Enderlein, E. Toprak, and P. R. Selvin, Opt. Express **14**, 8111 (2006).
8. S. Stallinga, J. Opt. Soc. Am. A **32**, 213 (2015).
9. C. S. Smith, N. Joseph, B. Rieger, and K. A. Lidke, Nat Meth **7**, 373 (2010).
10. A. Meiri, C. G. Ebeling, J. Martineau, Z. Zalevsky, J. M. Gerton, and R. Menon, Opt. Express **25**, 17174 (2017).
11. C. G. Ebeling, A. Meiri, J. Martineau, Z. Zalevsky, J. M. Gerton, and R. Menon, Nanoscale **7**, 10430 (2015).
12. E. Betzig, G. H. Patterson, R. Sougrat, O. W. Lindwasser, S. Olenych, J. S. Bonifacino, M. W. Davidson, J. Lippincott-Schwartz, and H. F. Hess, Science **313**, 1642 (2006).
13. S. T. Hess, T. P. K. Girirajan, and M. D. Mason, Biophys. J. **91**, 4258 (2006).
14. G. Shtengel, J. A. Galbraith, C. G. Galbraith, J. Lippincott-Schwartz, J. M. Gillette, S. Manley, R. Sougrat, C. M. Waterman, P. Kanchanawong, M. W. Davidson, R. D. Fetter, and H. F. Hess, Proc. Natl. Acad. Sci. **106**, 3125 (2009).
15. M. F. Juette, T. J. Gould, M. D. Lessard, M. J. Mlodzianoski, B. S. Nagpure, B. T. Bennett, S. T. Hess, and J. Bewersdorf, Nat Meth **5**, 527 (2008).
16. M. J. Rust, M. Bates, and X. Zhuang, Nat Meth **3**, 793 (2006).
17. B. Huang, W. Wang, M. Bates, and X. Zhuang, Science **319**, 810 (2008).
18. E. Mukamel, H. Babcock, and X. Zhuang, Biophys. J. **102**, 2391 (2012).
19. S. W. Hell and J. Wichmann, Opt. Lett. **19**, 780 (1994).
20. B.-C. Chen, W. R. Legant, K. Wang, L. Shao, D. E. Milkie, M. W. Davidson, C. Janetopoulos, X. S. Wu, J. A. Hammer, Z. Liu, B. P. English, Y. Mimori-Kiyosue, D. P. Romero, A. T. Ritter, J. Lippincott-Schwartz, L. Fritz-Laylin, R. D. Mullins, D. M. Mitchell, J. N. Bembenek, A.-C. Reymann, R. Böhme, S. W. Grill, J. T. Wang, G. Seydoux, U. S. Tulu, D. P. Kiehart, and E. Betzig, Science. **346** (2014).
21. Y. Shechtman, L. E. Weiss, A. S. Backer, S. J. Sahl, and W. E. Moerner, Nano Lett. **15**, 4194 (2015).
22. Y. Shechtman, A.-K. Gustavsson, P. N. Petrov, E. Dultz, M. Y. Lee, K. Weis, and W. E. Moerner, Biomed. Opt. Express **8**, 5735 (2017).
23. G. Grover, K. DeLuca, S. Quirin, J. DeLuca, and R. Piestun, Opt. Express **20**, 26681 (2012).
24. M. A. Thompson, J. M. Casolari, M. Badieirostami, P. O. Brown, and W. E. Moerner, Proc. Natl. Acad. Sci. **107**, 17864 (2010).
25. S. R. P. Pavani and R. Piestun, Opt. Express **16**, 22048 (2008).
26. S. R. P. Pavani, M. A. Thompson, J. S. Biteen, S. J. Lord, N. Liu, R. J. Twieg, R. Piestun, and W. E. Moerner, Proc. Natl. Acad. Sci. **106**, 2995 (2009).
27. S. Jia, J. C. Vaughan, and X. Zhuang, **8**, 302 (2014).
28. A. S. Backer, M. P. Backlund, A. R. v. Diezmann, S. J. Sahl, and W. E. Moerner, Appl. Phys. Lett. **104**, 193701 (2014).
29. W. Wang, H. Shen, B. Shuang, B. S. Hoener, L. J. Tauzin, N. A. Moringo, K. F. Kelly, and C. F. Landes, The J. Phys. Chem. Lett. **7**, 4524 (2016).
30. J. Broeken, B. Rieger, and S. Stallinga, Opt. Lett. **39**, 3352 (2014).
31. C. Smith, M. Huisman, M. Siemons, D. Grünwald, and S. Stallinga, Opt. Express **24**, 4996 (2016).
32. Y. Shechtman, L. E. Weiss, A. S. Backer, M. Y. Lee, and W. E. Moerner, Nat. Photonics **10**, 590 (2016).
33. E. Hershko, L. E. Weiss, T. Michaeli, and Y. Shechtman, arXiv:180701637 (2018).
34. M. N. Bongiovanni, J. Godet, M. H. Horrocks, L. Tosatto, A. R. Carr, D. C. Wirthensohn, R. T. Ranasinghe, J.-E. Lee, A. Ponjavic, J. V. Fritz, C. M. Dobson, D. Klenerman, and S. F. Lee, **7**, 13544 (2016).
35. .
36. J. W. Goodman, *Introduction to Fourier Optics*, Physical and Quantum Electronics Series (McGraw Hill, 1968), 1st ed.
37. H. KIRSHNER, F. AGUET, D. SAGE, and M. UNSER, J. Microsc. **249**, 13 (2013).
38. R. Cools and K. J. Kim, J. Appl. Math. Comput. **7**, 477 (2000).
39. J. Lagarias, J. Reeds, M. Wright, and P. Wright, SIAM J. on Optim. **9**, 112 (1998).
40. R. J. Ober, S. Ram, and E. S. Ward, Biophys. J. **86**, 1185 (2004).
41. J. Chao, S. Ram, T. Lee, E. S. Ward, and R. J. Ober, Opt. Express **23**, 16866 (2015).
42. A. S. Backer and W. E. Moerner, The J. Phys. Chem. B **118**, 8313 (2014).
43. A. S. Backer, M. P. Backlund, M. D. Lew, and W. E. Moerner, Opt. Lett. **38**, 1521 (2013).
44. Y. Shechtman, S. J. Sahl, A. Backer, and W. Moerner, Phys. Rev. Lett. **113**, 133902 (2014).
45. J. T. Martineau, R. Menon, E. M. Jorgensen, and J. Gerton, Microsc. Microanal. **25**, 1232–1233 (2019).
46. S. Fernando, J. Martineau, E. Jorgensen, and J. Gerton, Microsc. Microanal. **27**, 864–867 (2021).